STUDIES OF HIGH-LATITUDE THERMOSPHERE UTILIZING OPTICAL INSTRUMENTS

YOUNG-IN WON[1], YOUNG-MIN CHO[1], AND YONG-HA KIM[2]

[1]Polar Sciences Laboratory, Korea Ocean R & D Institute
[2]Department of Astronomy and Space Science, Chungnam National University
E-mail: yiwon@kordi.re.kr

ABSTRACT

The investigation of the space environment requires the use of experimental and theoretical tools and resources in order to perform the research task. Understanding of these research tools is imperative for proper interpretation of the results. In this paper, we discuss on research tools that are widely used in the field of aeronomy; Fabry-Perot interferometer and Michelson interferometer. These instruments have been used extensively as passive optical devices, spectrally monitoring the natural atmospheric emissions (airglow). This function has made both instruments valuable tools in upper atmospheric studies since they provide the ability to determine the dynamic and thermodynamic properties of the upper atmosphere by monitoring naturally-occuring emission.

Keywords: thermosphere, upper atmosphere, interferometer, airglow

I. INTRODUCTION

Since the start of the Space Age, our knowledge of the near-Earth space environment has increased significantly. The desire to investigate and understand the space environment is no longer driven by intellectual curiosity only, but there has been increasing concern and interests about the variability, both natural and artificial, of the Earth's upper atmosphere. The effect of long term variations in solar activity and solar-driven disturbances on the upper atmosphere has lead to instances of premature re-entry of orbital vehicles, increased drags on satellites in low Earth orbit and disruption of radio communication. These and other effects such as radiation and material damage, satellite charging, single-event upsets, and induced ground currents all fall into a class now called space weather phenomena. The absorption of variable solar ultraviolet and X-ray radiation not only heats the atmosphere, but also initiates chains of photo-chemical reactions that ionizes the upper atmosphere, forming the ionosphere. Therefore both the upper atmosphere and ionosphere are important to space weather not only because adverse effects commonly occur, but also because they are strongly coupled to each other and to other regions of space.

The Earth's thermosphere, where the neutral gas temperature increases towards an asymptotic value determined by the variable sources of solar heating, occupies the altitude region between about 90-600 km and spans the region from the coldest part of the atmosphere to the hottest. The dynamical, thermodynamical and compositional state of the thermosphere depends on solar EUV and UV heating, various dynamical forcings and neutral-plasma interactions, with neutral winds inducing diffusive changes on composition and adjusting to, and thereby modifying, the pressure gradients due to temperature variations. The high-latitude thermosphere is different than that at middle and low latitudes due to the direct and indirect influence of high-latitude magneto-spheric/ionospheric processes. These processes are essentially driven by the solar wind whose variations in bulk velocity, number density, and magnetic field give rise to complex interactions with the magnetosphere. The ionosphere is electrically coupled with the magneto-sphere by highly conductive vertical magnetic field lines which pervade the ionosphere at high-latitudes. Therefore, the effect of the solar and geomagnetically driven fluctuations to neutral particles are revealed most distinctly in high-latitude.

The thermosphere is distinguished from its neighbours from the fact that it is regions where most radiations from the atmospheric atoms and molecules in the visible spectrum (i.e., the airglow and the aurora) originate. Airglow is irradiance caused by atomic and molecular radiative transitions. Most of the atmospheric spectroscopic radiations originate in the thermosphere because

it is the region where most of the solar UV and EUV (Extreme UV) energetic photons are absorbed. The radiation out from the thermosphere in the visible, UV and IR portions of the spectrum accounts for only a small fraction of the energy that is absorbed, but the spectral lines and bands are invaluable means for remotely sensing several physical properties and processes in the emitting regions. Analysis of various emission features has yielded insight into chemical processes, energy balance and the dynamic behavior of the upper atmosphere. Many observational techniques are available for investigating the physical properties of the upper thermosphere. These techniques include satellite and ground-based optical measurements of the airglow and incoherent scatter radar techniques (Evans 1975). The radar techniques have been used extensively for investigating the behavior of the ionized component of the thermosphere. In this paper, we will focus on the basic concepts and principles of two most widely used optical instruments (Fabry-Perot interferometer and Michelson interferometer) for the passive remote sensing of the thermosphere.

II. FABRY-PEROT INTERFEROMETER (FPI)

In the last years of the 19th century two young French physicists at the University of Marseilles, Alfred Perot and Charles Fabry, described a novel form of interference device. This device made use of interference phenomena due to waves successively reflected between two thinly silvered plane glass plates set accurately parallel. These semi-transparent mirrors separated by a fixed distance is called an "etalon" or interference gauge. The FPI, originally used for the spectroscopic determination of the standard meter, has been recognized by many as an optical device capable of numerous applications. In the field of aeronomy, Babcock (1923) first attempted to determine upper atmospheric properties by observing the naturally occurring [OI] 5577 Å radiation in the night sky with a ground-based FPI. Because of the low effective efficiency of the photographic technique used, the results were poor. With the progress in detector technology, the FPI gained its reputation as one of the most powerful optical instruments in atmospheric studies. Dynamic and thermodynamic properties of the atmosphere can be determined from the Doppler shift and width of the electromagnetic radiation emitted by various atmospheric species as a result of natural processes. The FPI has been used extensively as a passive optical device, in particular after Armstrong (1968, 1969) reported the feasibility of measuring winds as well as temperatures by observing the [OI] 6300 Å emission. The thermospheric emission line at 6300 Å of atomic oxygen was first observed in the laboratory by

Paschen (1930). This line is "forbidden" and not easily seen in the laboratory due to the difficulty of and keeping the excited state from being quenched through collisions with other atoms or molecules of the sides of the chamber. The principal processes for production and loss of $O(^1D)$ in the upper atmosphere are: photodissociation of O_2, impact of fast electrons on atomic oxygen, and dissociative recombination. The volume emission rate (photons/cm^3/sec) for the 6300 emission is strongly peaked at an altitude of about 240 km, with a half thickness of about 50 km. At the peak altitude, the $O(^1D)$ atom is in local thermodynamic equilibrium with the ambient neutral gases, because the lifetime of the $O(^1D)$ metastable state of 110 seconds is far greater than the collision times of about 1 to 2 seconds. Therefore, the $O(^1D)$ atom can be used as a tracer to provide the bulk velocity and kinetic temperature of the thermosphere. A summary of the present status of Fabry-Perot devices (in the laboratory and their applications in geophysics, astronomy, and laser spectroscopy) can be obtained from Hernandez (1986).

(a) Mathematical Development

Consider a plane-parallel transparent plate of refractive index n', and suppose that a plane wave of monochromatic light is incident upon the plate at angle θ (Figure 1). At the first surface this wave is divided into two
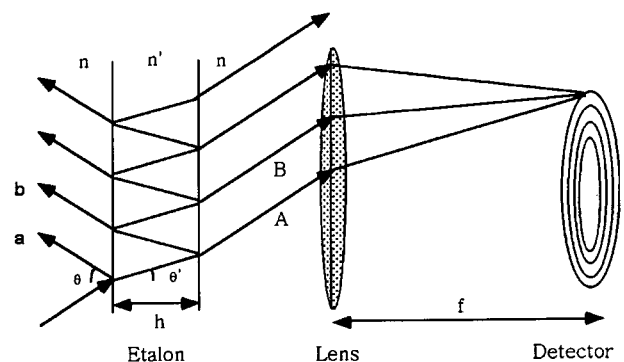

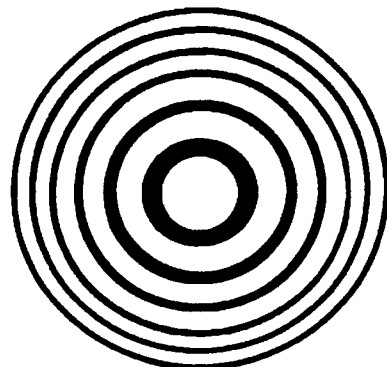Fig. 1. Multiple-beam interference in a Fabry-Perot interferometer

Fig. 2. Fabry-Perot interferometer ring patterns at the focal plane.

plane waves, one reflected (indicated by the ray leading to a) and the other transmitted. The division process of the wave remaining inside the slab continues as indicated in the Figure 1.

The phase difference d, between two emerging waves, A and B, or a and b is given by

$$d = 4\pi n' h \cos \theta' / \lambda_0 \qquad (1)$$

where n' is the refractive index of the plane-parallel transparent plate, h is the thickness of the plate, θ' is the angle of the internal rays with respect to the optical axis, and λ_0 is the wavelength in a vacuum. Constructive interference occurs when the following condition is met,

$$4\pi n' h \cos \theta' / \lambda_0 = 2\pi m$$
or
$$2 n' h \cos \theta' / \lambda_0 = m \qquad (2)$$

where m is called the order of interference.

A converging lens gathers the transmitted light and brings it to a focal plane on a detector. For a monochromatic incident light beam, the transmitted light forms a series of concentric rings on the focal plane (Fig. 2). Each ring corresponds to the transmission maxima (constructive interference) or minima (destructive interference).

The transmittance function of a FPI with perfectly flat surfaces exactly parallel to each other is given by the Airy function (Born & Wolf 1975; Hernandez 1986), where R is the reflectivity of the dielectric coating:

$$T_e(\lambda, \theta) = \frac{(1-R)^2}{1 - 2R\cos\left\{2\pi\frac{2n'h}{\lambda}\cos\theta'\right\} + R^2}$$

$$= \frac{1-R}{1+R}\left\{1 + 2\sum_{n=1}^{\infty} R^n \cos\left(\frac{4\pi n'h}{\lambda}n\cos\theta'\right)\right\} \qquad (3)$$

The Airy transmittance function is plotted in Fig. 3, as a function of the phase retardation of the beams for various reflectivities indicated by the various curves. Each peak here corresponds to a different order of interference and the values of the reflectivities are; 0.98, 0.81, 0.65, and 0.45 from the narrowest profile to the widest one. As the reflectivity increases, the instrumental resolution or the ability to separate closely spaced lines also increases.

The free spectral range, the distance between two neighboring peaks is defined as

$$\Delta\lambda_0 = \frac{\lambda_0}{m} = \frac{\lambda_0^2}{2n'h\cos\theta'} \qquad (4)$$

Physically, $\Delta\lambda_0$ means the change in wavelength required to move one transmission peak to the next one. The sharpness of the fringe is defined by measuring the
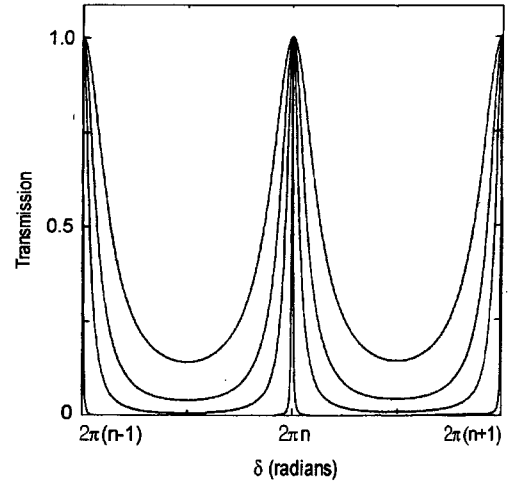

Fig. 3. The Airy transmittance as a function of the phase retardation of the beams for various reflectivities (Born & Wolf 1975).
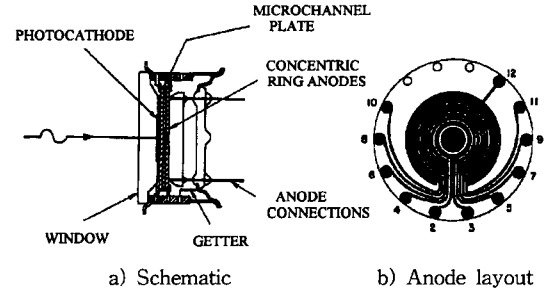

a) Schematic   b) Anode layout

Fig. 4. Image plane detector, a) Internal structure, b) anode layout. (from Killeen et al. 1983).

"full-width at half maximum (FWHM)" where the intensity has dropped to half its maximum value. The finesse of the etalon, $f = \Delta\lambda_0/\text{FWHM}$ determines the spectral resolution of the measurement.

The Image Plane Detector (IPD) has been used as a detector in various FPIs including the DE-2 (Dynamics Explorer-2) FPI. The IPD is an electro-optical device that converts the intensity distribution of light falling on the image plane into a set of discrete electron pulses. Fig. 4 shows the schematic diagram of an IPD (from Killeen et al. 1983). The device has a 12 mm effective diameter face plate on which a photo-cathode is placed. Three micro channel plate (MCP) electron multipliers are behind the photo cathode which provide a gain of 106 electrons. The segmented anode, which is composed of 12 concentric rings of equal area, collects the output of the MCP chain. Currently, IPDs are being used in the Thule Air Base and Søndre Strømfjord FPIs. A complete description is given in Killeen et al. (1983).

(b) Retrieval of Geophysical Parameters

The interference pattern imaged on the detector of an FPI contains geophysical parameters of interest in the measurement line of sight. Assuming that the gas is in

thermodynamic equilibrium with a Maxwellian velocity distribution, winds and temperatures can be deduced from the atmospheric emissions.

The Maxwellian velocity distribution is given by

$$f(v) = \left(\frac{2\pi kT}{m}\right)^{1/2} \exp\left[\frac{-m(v-\bar{v})^2}{2kT}\right] \qquad (5)$$

where m and T are the mass and the temperature of the emitting gas, k is the Boltzmann constant, v and $\bar{v}$ are velocity and bulk velocity of gas, respectively. Because we are dealing with the line-of-sight wind, the equation above is written in one-dimensional form. The Gaussian emission source function, which is proportional to the fraction of 'particles' with the corresponding velocity $f(v)dv$ is expressed as

$$Y(\lambda) = \left(\frac{c^2}{\lambda_l^2}\frac{2\pi kT}{m}\right)^{1/2} \exp\left[\frac{-m}{2kT}\left(\frac{\lambda-\lambda_l}{\lambda_l/c}\right)^2\right]$$

$$\cong \left(\frac{c^2}{\lambda_o^2}\frac{2\pi kT}{m}\right)^{1/2} \exp\left[\frac{-m}{2kT}\left(\frac{\lambda-\lambda_o-\Delta\lambda}{\lambda_o/c}\right)^2\right] \qquad (6)$$

where c is speed of light, λ_o is the center wavelength of the emission, and λ_l is the spectral location of the shifted emission. Then, the line-of-sight wind can be determined by measuring the Doppler shift
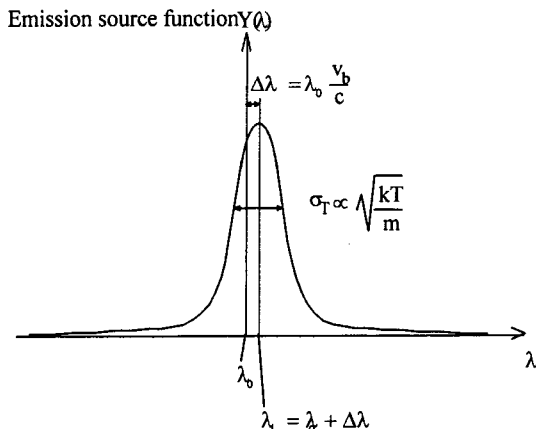
$$V = \frac{c(\lambda_l - \lambda_o)}{\lambda_o} \qquad (7)$$

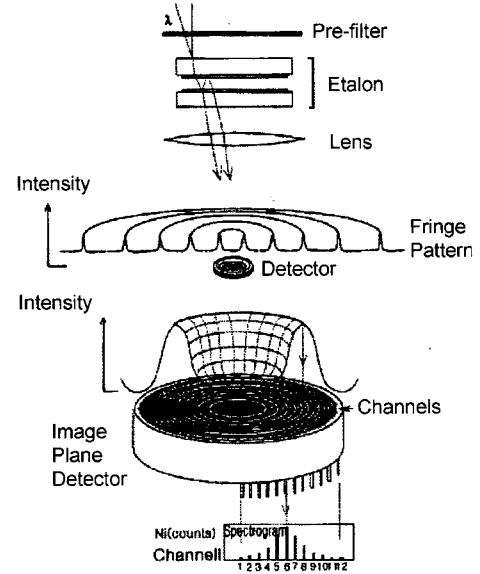For a Maxwellian distribution, the FWHM of the source profile is related to the species temperature.

$$\sigma_T = 2\left(\frac{2kT\ln 2}{m}\right)^{1/2}\frac{\lambda_o}{c} \qquad (8)$$

Fig. 5 shows the shift and width of an emission line, and their relationship to the bulk velocity and the kinetic temperature.

The interference fringe produced by the etalon is focused onto the detector. The group of responses from

Fig. 6. This illustrates how the fringe that is produced by the etalon is imaged to the detector. All that is needed to obtain wind and temperature is a radial 'cut' of an order of the fringe. The multichannel detector makes use of all azimuthal angles of the order, for increased signal, and samples the entire fringe simultaneously for greater temporal resolution.
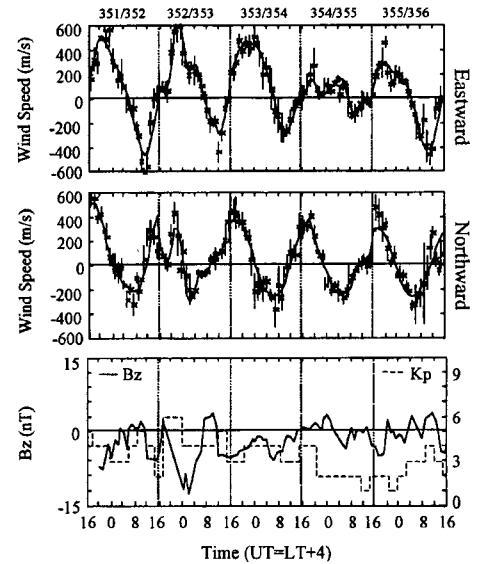

Fig. 7. Hourly-averaged thermospheric winds near 240-km altitude measured above Thule, Greenland during a cloud-free 5-day period in 1988. The solid lines in the upper two panels represent cubic spline fits and the error bars are calculated standard deviation (from Killeen et al. 1995).

the detector's channels is called a spectrogram and forms the basic unit of information from which geophysical data are extracted. The essential principle of the FPI is to transform the spectral distribution of an emission line into a radial distribution, in the form of a FPI spectrogram, so that the spectral distribution can be measured directly by the detector.

Emission source function $Y(\lambda)$

$\Delta\lambda = \lambda_o\dfrac{v_b}{c}$

$\sigma_T \propto \sqrt{\dfrac{kT}{m}}$

$\lambda_l = \lambda_o + \Delta\lambda$

Fig. 5. The Gaussian distribution of a thermally broadened and Doppler-shifted emission line.

Fig. 6 schematically shows a broad overview of the process that results in a measured spectrogram. The experimentally measured spectrogram represents a discretized approximation to the expected Gaussian emission line source, convolved with the instrument transfer function. Knowing the instrument transfer function, the spectrogram can be de-convolved to yield some important geophysical parameters such as wind, temperature, surface brightness, and continuum brightness. The instrumental transfer function can be determined either analytically or experimentally. The analytic form of the instrument function is given by convolving the individual analytic functions for specific instrumental broadening effects. This convolution has been discussed by Hays & Roble (1971). There are a number of problems with this approach since it is difficult to discuss all possible broadening effects by analytic expressions. The experimental approach has the advantage that it derives the actual instrument transfer functions. The instrument transfer function represents the relative sensitivity of each detector channel and contains all the etalon and optical defects in the system. The shape of the instrument transfer function can be obtained from an instrument calibration procedure. A frequency-stabilized He-Ne laser is used to provide a line source of negligibly small thermal width and continuum background. Then, each channel response is recorded during a careful scan of the instrument over approximately two free spectral ranges. The instrument scan is performed by changing pressure within the etalon chamber at finite increments. The detailed procedures of obtaining the instrumental response and the de-convolution for extracting geophysical parameters are referred to Killeen & Hays (1984).

(c) Observation

Fig. 7 shows an example of zonal and meridional winds from [OI] 6300 Å measurement using the method described above. Measurements were made at Thule (76.5°N, 69.0°W, Λ=86), Greenland, using an automated FPI operated by Space Physics Research Laboratory, University of Michigan. The data were taken during a 5-day period of clear skies during solar maximum conditions and averaged into 1-hour bins. The data of Fig. 7 illustrate typical upper thermospheric (~240 km) winds as measured in the central geomagnetic polar cap during solar maximum conditions ($F_{10.7}$=230). The first-order wind dependence is one of simple diurnal rotation of the wind vector pointing in the approximately antisolar direction. This sinusoidal nature of the observations is interrupted occasionally by transient deviations. An example of such a perturbation occurs near 16:00 UT on day 352, when the meridional wind abruptly changed from blowing northward at ~100 ms^{-1} to having a very
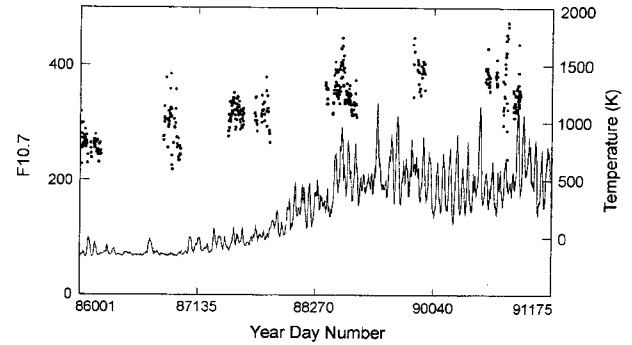

Fig. 8. Daily-averaged neutral thermospheric temperatures measured at Thule Air Base as a function of year day number between 1986 and 1991. The figure also the corresponding solar EUV flux index ($F_{10.7}$) for the period.

small magnitude for about 4 hours before returning to a northward speed of ~80 ms^{-1}. This perturbation appears as a "bite-out" in the sinusoidal variation associated with antisunward flow. Fig. 7 also shows the variations of the geomagnetic index Kp and the north-south component of the interplanetary magnetic field (IMF Bz). This bite-out in the meridional wind near 16:00 UT on day 352 is associated with a similar disruption in the zonal wind profile and correlates in time with a brief northward turning of the IMF. We ascribe this and other perturbation from the simple diurnal sinusoidal signature to be due to the changed ionospheric convection pattern (and hence changed ion drag forcing of the neutral wind) during the short period of positive Bz (northward). This dependence of the polar cap wind on the sign of the IMF Bz is consistent with previous work (Niciejewski et al. 1994).

Fig. 8 shows the daily averaged neutral temperatures from Thule as a function of time over the 6-year observing period. The figure also shows the $F_{10.7}$ solar index for the same period. As can be seen, the polar cap upper thermospheric temperature is a strong function of solar cycle rising from values of near 500 K at solar minimum to values in excess of 1800 K at solar maximum. The large amount of day-to-day variability evident in these data is primarily due to the effects of geomagnetic activity.

III. MICHELSON INTERFEROMETER (MI)

Recently, there has been a marked improvement in the techniques for measuring the lower thermospheric temperatures by observing a number of OH vibration-rotation bands (Meinel bands) as well as O_2 molecular bands. The hydroxyl (OH) emissions were first identified by Meinel (1950). Since then, many researchers have made ground-based, and rocket-borne observations of individual OH vibrational- rotational bands and identified its peak altitude at 87±3 with a half width 5~8 km
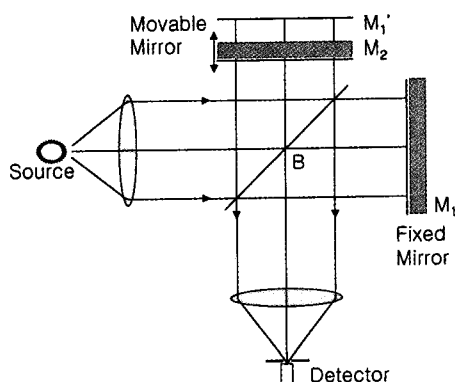
Fig. 9. A simple schematic displaying the basic components of a Michelson Interferometer.

Table 1. The specification of Bomem Michelson interferometer

Spectral range	5000 cm^{-1} to $10,000 \text{ cm}^{-1}$ (detector response)
Resolution	1, 2, 4, 8, 16 cm^{-1} (selectable)
Detector	0.5 mm diameter InGaAs detector module (TE cooled operation)

Fig. 10. An atmospheric OH spectrum recorded at Ansan. Interferograms over about a 5-minute period (50 interferograms) were co-added to get this spectrum (from Won et al. 1999a).
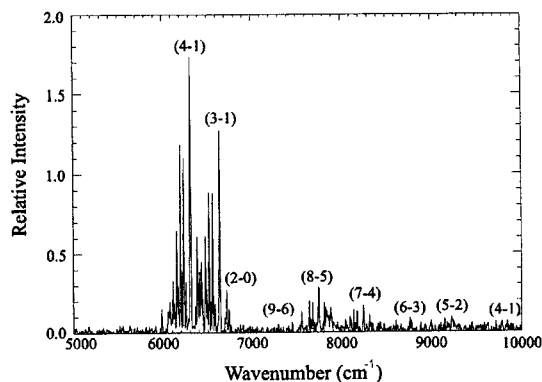
(Baker & Stair 1988). Because rotational relaxation is sufficiently rapid in this region, the distribution of rotational lines within a band is expected to represent the kinetic temperature of the gas. Ground-based measurements of the OH rotational lines therefore provide the atmospheric temperature at this height. Advances in Fourier transform spectrometry have enabled a number of OH vibration-rotation bands (Meinel bands) to be monitored from the ground. The molecular bands of the Meinel system of the OH radical appear beyond about 5200 Å and originate from the lower thermospheric/ upper mesospheric region (~87 km) of the Earth. Advances in the production of solid-state detectors and obtaining a broader spectral range have contributed significantly to the MI becoming the instrument of choice for infra-red observations of atmospheric emissions. Rotational temperatures are obtained from measurements of the OH molecular bands of the (3-1) transitions.

(a) Basic Theory

The schematic of a simple MI is shown in Fig. 9. Light from the source (S) is incident on a 45° partially reflective glass plate (B). At B the light is split into two beams; one transmitted to fix mirror (M_1) and the other one to the movable mirror (M_2). Mirrors M_1 and M_2 are mutually perpendicular. A virtual image of M_1 exists, parallel to M_2 as shown in the diagram as M_1'. These two planes constitute a virtual plane-parallel layer of optical thickness equal to twice the optical path difference (χ) between plate B and M_1 and plate B and M_2. Mirror M_2 is capable of moving perpendicularly to the incident beam, thereby increasing or decreasing χ between the two beams. The two combining beams will interfere constructively or destructively depending on the value of χ and the resultant interference pattern as a function of χ will be measured by the detector, called the interferogram. Then, the spectrum of the incident light can be calculated from the interferogram by taking

the fourier transform.

(b) OH Airglow Spectrum (Meinel bands)

Fig. 10 shows an example of the calculated spectrum of the night sky recorded at Ansan on August 29, 1998, by using a MI. This interferometer was manufactured by Bomem Inc., Canada. Individual interferograms could be acquired with about a 5-second temporal resolution. In order to increase the signal-to-noise ratio, we needed to co-add a number of interferograms. However, increasing the number of interferograms reduces the temporal resolution and, therefore, a compromise should be reached between the increase in the S/N ratio and the reduction in the temporal resolution. For our calculation, interferograms over about a 5-minute period (50 interferograms) were co-added. The resultant set of interferograms was truncated with a cosine apodization function, and then a fast Fourier transform was performed. The resultant spectra were then corrected for the detector sensitivity which was determined by using an absolute intensity calibration. An absolutely calibrated lamp was supplied from the manufacturer for this purpose. The system had a wavenumber precision of 0.01 cm^{-1} which was determined by an internal He-Ne laser. The interferometer scan arm, the sampling of the interferogram, and the data acquisition were all controlled by a personal computer. A scope was attached to the system to acquire the atmospheric emission from the sky. Table 1 briefly describes the specifications of the system.

From Fig. 10, it is noted that bands (3-1) and (4-2) are the most intense in this spectrum; atmospheric atten-
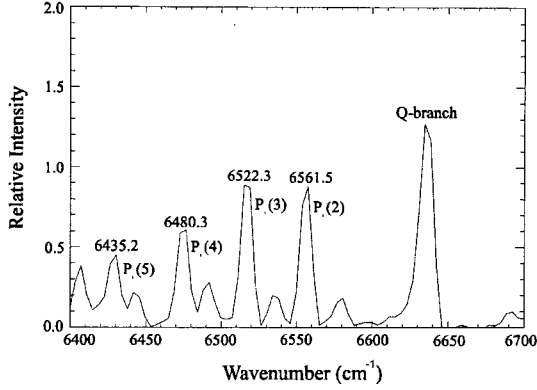
Fig. 11. An enlarged portion of Fig. 10 showing the vibrational-rotational lines used to determine the total band intensity and the temperature (from Won et al. 1999a).

uation reduces the intensity of other bands. The (4-2) lines are not used in our temperature calculation due to a significant change in the spectral response of the In-GaAs detector in that region. Fig. 11 is the same spectrum as Fig. 10, but shows an enlarged portion of the (3-1) P_1 rotational lines to be used for the temperature determination. The spectral line centered at approximately 6434 cm^{-1} is, in fact, two overlapping spectral lines, one at 6435.2 cm^{-1} [(3-1)P_1(5)] and the other at 6433.6 cm^{-1} [(4-2)R_1(4)]. For this reason, the (3-1)P_1(5) line was not used in our temperature calculation.

The hydroxyl radicals have radiative lifetimes of 4-6 milliseconds (Mies 1974). Because molecules in the mesopause (~80 km) have collision times of 6.6×10^{-5} seconds or collision frequencies of about 15 per millisecond, OH radicals will have an average of 75 collisions before they decay to a lower state, which is enough to thermalize their rotational distributions (Krassovsky et al. 1977; Turnbull & Lowe 1983). Therefore, the excited OH molecules are in local thermodynamic equilibrium, and their rotational distribution will conform to a Boltzmann distribution. This thermalization of the rotational states is fundamental to the calculation of temperatures from hydroxyl emission spectra. Because the majority of photon emission originates from the peak of the OH* layer, the rotational temperature is assumed to be an accurate representation of the neutral atmospheric temperature at the peak altitude (Sivjee et al. 1987).

(c) Determination of rotational temperatures

For a Boltzmann distribution of multiplet rotational levels, the photon emission intensity is given by the following expression (Mies 1974):

$$I_{(J', v' \to J'', v'')} = N_{v'}A_{(J', v' \to J'', v'')} \frac{2(2J' + 1)}{Q_{v'}(T_{rot})}e^{\frac{-E_{J'}}{kT_{rot}}} \quad (9)$$

where J' is the upper-state total angular momentum, I is

the intensity of the vibrational-rotational transition from the state J', v' to the state J'', v'', k is the Boltzmann constant, $N_{v'}$ is the total concentration of molecules in the upper vibrational state, $A(J', v' J'', v'')$ is the spontaneous Einstein emission coefficient for the vibrational-rotational transition, which is the reciprocal of the expected lifetime of a particular state, and $Q_{v'}$ is the partition function or state sum defined as

$$Q_{v'}(T) = \sum_J (2J' + 1)e^{\frac{-E_{J'}}{kT_{rot}}} \quad (10)$$

Here, $E_{v'}(J')$ is the upper state energy. The energy of a state, or its term value, is usually given in units of reciprocal centimeters (cm^{-1}) and is denoted by $F_{v'}(J')$, and $E_{v'}(J')=F_{v'}(J')*100\ hc$, where h is Planck's constant and c is the speed of light.

Rearranging and taking the natural logarithm of Eq. (9), we obtain the following relationship:

$$\ln\left[\frac{I_{(J', v' \to J'', v'')}}{2(2J' + 1)A_{(J', v' \to J'', v'')}}\right]$$

$$= \ln\left[\frac{N_{v'}}{Q_{v'}(T_{rot})}\right] - \frac{-F_{v'}(J')100hc}{kT_{rot}} \quad (11)$$

This equation is a linear equation of the form $y=mx+b$ with a slope of 100 hc/kT_{rot}. The slope is inversely proportional to the rotational temperature (T_{rot}), and the intercept, $\ln[N_{v'}/Q_{v'}]$, is related to the overall band intensity. A plot of the left-hand side of Eq. (11) versus $F(J')$ yields a straight line. The rotational temperature, T_{rot}, is determined from the slope of this line because the slope corresponds to 100 hc/kT. The Einstein coefficients and the theoretically calculated rotational term values, $F_{v'}(J')$, to be used in our calculation are taken from Mies (1974). The intensities of the peaks are calculated by fitting the peak profiles. From the intercept of the graph, which equals $\ln(N_{v'}/Q_{v'})$, the total number of molecules with an upper vibrational level of $N_{v'}$ may be obtained since the temperature dependent $Q_{v'}(T)$ is known (Krassovsky et al. 1962). The total band intensity of the (3-1) band can be obtained from $I_{3-1} = N_3A_{3-1}$ (Hecht et al. 1987), where A_{3-1} is the Boltzmann-averaged Einstein coefficient for all transitions in the (3-1)
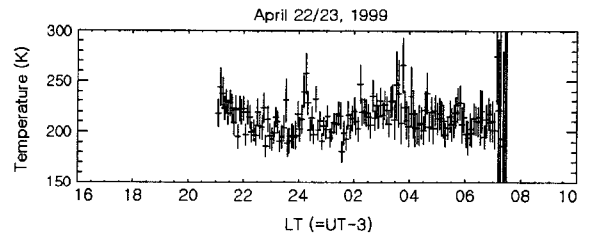
Fig. 12. A plot of rotational temperature measured on the night of April 22, 1999 with error bars (statistical uncertainties) superimposed.
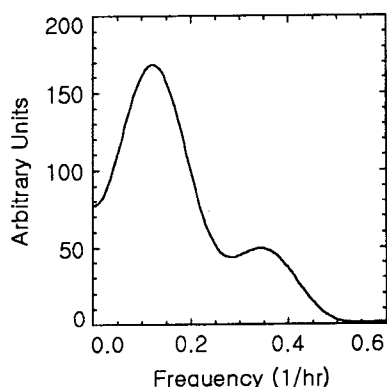
Fig. 13. Power spectral density of OH rotational temperature for Fig. 12 (from Won et al. 2000).

band, is temperature independent over the range of lower thermospheric temperatures, and has a value of 39.93 s^{-1} (Mies 1974).

(d) Observation

The MI was installed at King Sejong station (62.22°S, 301.25°E), Antarctica in February 1999, and has been in routine operation, making zenith measurements of the Meinel OH (3-1) band. Intensive operational efforts have been made since April, 1999 with observations only limited by the weather conditions. One sample result from our MI is shown in Fig. 12, a plot of the rotational temperatures of OH (3,1) on the night of April 22, 1999, calculated using the method described above. The vertical lines represent uncertainties, indicating the passage of cloud during the time of observation near 03 UT and 06:30 UT and after 10UT. Despite the span of cloud cover from time to time, a visible oscillation in temperature is seen from the figure. These variations suggest the modulation of OH chemical and dynamical processes around the mesopause where the peak emission occurs. In order to quantify the frequency content, we have performed power spectral analysis of temperature and intensity on the data shown in Fig. 12. Before applying a spectral analysis, however, we eliminated those data during periods of cloud cover, then averaged the remaining data in 30-minute interval. By doing the 30-minute interval average, we could fill the gap resulted by the filtering process, and make the data evenly spaced.

Fig. 13 shows the power spectrum of temperature smoothed by a Tukey window. A large, distinct peak occurs around the 8-hr period. There have been various results reporting the existence of large amplitude variations in the Lower Thermosphere temperature and airglow brightness in low-order tidal periods (Sivjee & Walterscheid 1994, Won et al. 1999b, Pendleton et al. 2000). The classical migrating tide is not appropriate in

explaining the observed oscillations because its amplitude should be very small in the polar region (Forbes, 1982 a, b). Recently, Oznovich et al. (1997) raised a question on the gravity wave explanation of the observed 8-hr oscillations and suggested a need for a detailed inspection of the model with respect to various parameters such as lapse rate and minor constituent concentrations. Another possibility for the observed waves may be various natural oscillations between 7 and 10 hours in the lower thermosphere and upper mesosphere region, responding dominantly to the forces over a range of periods (Meyer & Forbes, 1997). Continuous measurements of OH intensity and the temperature over a year or longer are expected to reveal the detailed structure of atmospheric waves and their effects on the dynamical/ thermodynamical characteristics of the upper atmosphere.

IV. SUMMARY

We have described basic concepts and principles of two widely used optical instruments in the field of aeronomy; Fabry-Perot interferometer and Michelson interferometer. These instruments have been used extensively for the passive remote sensing of the upper atmosphere, especially the thermosphere where adverse effects related to space weather commonly occur. Even with the present and planned instruments, however, the data are sparse and there are many uncertainties in the physical and chemical processes that take place in the terrestrial upper atmosphere (and ionosphere). Therefore, a comprehensive understanding of the relevant inputs and internal processes is left as a major challenge for the development of reliable models of the atmospheric regions. Observations of the temperatures, winds, composition, and other important physical parameters should be monitored and continually compared against models in order to understand process in the space environment and the coupling to regions above and below. New ground- and space-based instruments, coupled with quantitative modeling, will provide a significant improvement in space weather specification and forecasting quality.

REFERENCES

Armstrong, E. B. 1968, Planet. Space Sci. 16, 16211
Armstrong, E. B. 1969, Planet. Space Sci. 17, 957
Babcock, H. D. 1923, ApJ 57, 209
Baker, D. J., & Stair Jr., A. T. 1988, Phys. Sci. 37, 611
Born, M., Wolf, E. 1975, Principles of optics, Pergamon Press
Evans, J. V. 1975, Rev. Geophys. Space Phys. 13, 887
Forbes, J. M. 1982a, J. Geophys. Res. 87, 5222
Forbes, J. M. 1982b, J. Geophys. Res. 87, 5241

Hays, P. B., & Roble, R. G. 1971, Applied Optics 10, 193

Hecht, J. L., Walterscheid, R. L., Sivjee, G. G., Christensen, A. B., & Pranke, J. B. 1987, J. Geophys. Res. 92, 6096

Hernandez, G. 1986, Cambridge Studies in Modern Optics: 3. Fabry-Perot Interferometers,(Eds. P. L. Knight and S. D. Smith, FRS) Cambridge University Press

Killeen, T. L., Kennedy, B. C., Hays, P. B., Symanow, D. A., & Ceckowski, D. H. 1983, Appl. Optics 22, 3503

Killeen, T. L., & Hays, P. B. 1984, Applied Optics 23, 612

Killeen, T. L., Won, Y.-I., Niciejewski, R. J., & Burns, A. G. 1995, J. Geophys. Res. 100, 21327

Krassovsky, V. I., Shefov, N. N., & Yarin, V. I. 1962, Planet. Space Sci. 9, 883

Krassovsky, V. I., Potapov, B. P., Semenov, A. I., Shagaev, M. V., Shefov, N. N., Sololev, V. G., & Toroshelidze, T. I. 1977, Ann. Geophys. 33, 347

Meinel, A. B. 1950, ApJ 111, 555

Meyer, C. K., & Forbes, J. M. 1997, Atmos. Sol. Terr. Phys. 59, 2185

Mies, F. H. 1974, J. Mol. Spectros. 53, 150

Niciejewski, R. J., Killeen, T. L., & Won, Y. 1994, J. Atmos. Terr. Phys. 56, 285

Oznovich, I., & Mc Ewen, D. J. 1997, J. Geophys. Res. 102, 4511

Paschen, F. 1930, Z. Phys. 65, 1

Pendleton, W. R., Taylor Jr., M. J., & Gardner, L. C. 2000, Geophys. Res. Lett. 27, 1799

Sivjee, G. G., Walterscheid, R. L., Hecht, J. H., Hamwey, R. M., Schubert, G., & Christensen, A. B. 1987, J. Geophys. Res. 92, 7651

Sivjee, G. G., & Walterscheid, R. L. 1994, Planet. Space Sci. 42, 447

Turnbull, D. N., & Lowe, R. P. 1983, Can. J. Phys. 61, 244

Won, Y.-I., Chung, J.-K., Lee, B. Y., Kim, Y., Kim, J., & Kim, J. B. 1999a, JKPS 34, 344

Won, Y.-I., Niciejewski, R. J., Killeen, T. L., Johnson, R. M., & Lee, B. Y. 1999b, J. Geophys. Res. 104, 25

Won, Y.-I., Cho, Y. M., Niciejewski, R. J., & Kim, J. 2000, Adv. Space Res., in press